Unveiling the Mechanisms Underlying Photothermal Efficiency of Gold Shell-Isolated Nanoparticles (AuSHINs) on Ductal Mammary Carcinoma Cells (BT-474)

Kobal, M. B.[1]; Camacho, S. A.[1,2]; Moreira, L. G.[1]; Toledo, K. A.[1,3]; Tada, D. B.[4]; and Aoki, P. H. B.[1]

[1] São Paulo State University (UNESP), School of Sciences, Humanities and Languages, Assis, SP, 19806-900, Brazil

[2] IFSC, São Carlos Institute of Physics, University of São Paulo (USP), São Carlos, SP 13566-590, Brazil

[3] São Paulo State University (UNESP), Institute of Biosciences, Letters and Exact Sciences, São José do Rio Preto, 15054-000, Brazil

[4] Institute of Science and Technology, Federal University of São Paulo (UNIFESP), São José dos Campos, SP, 12231280, Brazil.

* corresponding author: pedro.aoki@unesp.br

Abstract

Gold nanoparticles are valuable photothermal agents owing to their efficient photothermal conversion, photobleaching resistance, and potential surface functionalization. Herein, we combined bioinspired membranes with *in vitro* assays to elicit the molecular mechanisms of gold shell-isolated nanoparticles (AuSHINs) on ductal mammary carcinoma cells (BT-474). Langmuir and Langmuir-Schaefer (LS) films were handled to build biomembranes from BT-474 lipid extract. AuSHINs incorporation led to surface pressure-area (π-A) isotherms expansion, increasing membrane flexibility. Fourier-transform infrared spectroscopy (FTIR) of LS multilayers revealed electrostatic AuSHINs interaction with head portions of BT-474 lipid extract, causing lipid chain disorganization. Limited AuSHINs insertion into monolayer contributed to hydroperoxidation of the unsaturated lipids upon irradiation, consistently with the surface area increments of ca. 2.0%. In fact, membrane disruption of irradiated BT-474 cells containing AuSHINs was confirmed by confocal microscopy and LDH leakage, with greater damage at 2.2 x 10^{13} AuSHINs/mL. Furthermore, the decrease in nuclei dimensions indicates cell death through photoinduced damage.

Keywords: bioinspired tumoral membranes, BT-474 cell culture, photothermal therapy, plasmonic gold nanoparticles.

1. Introduction

Among the 19.3 million cancer cases diagnosed worldwide in 2018, more than 2 million were attributed to breast cancer, resulting in approximately 500,000 deaths among women.[1] As new cases emerged in 2020, the percentage of breast cancer diagnoses (11.7%) surpassed that of lung cancer (11.4%), with approximately 2.3 million cases and 690,000 deaths.[2] This resulted in breast cancer becoming the leading cause of death among women diagnosed with cancer.[3] Breast cancer can arise from various factors, including genetic and environmental disorders, family history, increased mammary density, obesity, or even a combination of several risk factors.[1,4] Ductal carcinoma *in situ* (DCIS) represents 25% of the diagnosed breast cancers,[5] which is characterized by the proliferation of neoplastic cells that remain confined within the mammary ducts.[4,6] Although typically not invasive, ductal carcinoma cells can sometimes escape and progress to invasive breast cancer in a subset of patients.[4,5] These tumors have the potential to metastasize, leading to morbidity and death in approximately 3% of patients initially diagnosed with DCIS.[1,4]

Conventional therapies for treating breast cancer, such as surgery, radiotherapy, and chemotherapy,[7] have been well stablished, but their non-selective activity in destroying cancer cells still poses a significant challenge.[3] In this scenario, photothermal therapy (PTT) has emerged as a promising approach due to its high selectivity, independence of oxygen, non-invasiveness, minimal drug resistance and low side effects.[8] In PTT, photothermal agents absorb light energy and generate heat, thereby increasing the temperature of the surrounding medium. Such mechanism allows for the selective targeting and destruction of cancer cells while preserving healthy cells, as tumors are more sensitive to high temperatures.[7,8]

Plasmonic nanoparticles of various compositions, shapes and structures have been applied in PTT owing to their bioavailability, biocompatibility, suitable size to promote enhanced penetration and retention effect in the tumor, high photothermal conversion efficiency and good photothermal stability.[7,8] Furthermore, such structures can sustain localized surface plasmon resonance (LSPR) when exposed to light, enhancing their absorption and scattering properties. Essentially, the electromagnetic field induces a coherent oscillation of the electrons in the conduction band of the metal, leading to the localized heating effect.[7–9] The most employed types of plasmonic nanostructures reported on literature are gold-based, including nanoshells, nanorods

(AuNRs), nanocages, nanostars (AuNS), and nanospheres (AuNPs). When compared to previously established non-metallic materials,[10] these plasmonic nanostructures exhibit superior photothermal properties, including the absence of photobleaching, handled synthesis and the versatility of surface functionalization.[11] For instance, surface modification with silica shell enabled the use of gold nanoparticles in biological medium, avoiding aggregation and therefore improving colloidal stability. Indeed, silica-coated AuNPs are known as gold shell-isolated nanoparticles (AuSHINs) and have been reported as effective surface-modified nanostructures for *in vitro* applications.[7]

In previous studies, we have used Langmuir films to hypothesize that the composition of cell membranes plays a central role in the incorporation of AuSHINs into tumor cells, as well as in the photothermal outcomes.[9,12] Indeed, Langmuir monolayers serve as effective models for mimicking cell membranes and studying interactions with biological systems at the molecular-level.[13] They have been extensively employed in diverse studies involving pharmaceutical drugs,[14–16] photosensitizers (PSs)[17,18] and metallic nanoparticles.[9,19] In this manuscript, we broaden the scope of these investigations by elucidating the binding mechanisms and photoinduced effects of AuSHINs on bioinspired cellular membranes of ductal mammary carcinoma cells (BT-474), using Langmuir and Langmuir-Schaefer (LS) films. As we shall demonstrate with FTIR data, the molecular-level interactions driving the AuSHINs insertion into the lipid membranes play a significant role in the photochemical outcome and efficiency in the *in vitro* experiments with BT-474 cells.

2. Experimental section

2.1. Synthesis and characterization of gold shell-isolated nanoparticles

Gold shell-isolated nanoparticles (AuSHINs) were synthesized as described by Grabar et al.[20] and Aroca et al.[21] Gold cores were prepared by adding 7.5 mL of sodium citrate (38.8 mmol/L) to 150 mL of boiling tetrachloroauric acid ($HAuCl_4$ 0.5 mmol/L) under vigorous stirring. After the color change from yellow to reddish purple, the solution was stirred for 10 min. Then, the heating was turned off and the colloidal suspension was kept under stirring for more 15 min, cooled and stored at room temperature. For the silica coating, 100 mL of AuNPs were mixed with 6 mL of fresh APTMS ((3-aminopropyl) trimethoxysilane, 1 mmol/L) solution followed by the addition of 12 mL of sodium silicate solution (0.54 %; pH = 10, adjusted with HCl 0.01 mol/L). Afterward, the heating was turned on and the temperature was kept between 90-95°C for 3 h. A colloidal aliquot was taken every 1 h for monitoring the silica coating via UV-Vis absorption spectroscopy using a Varian spectrophotometer (Cary 60 / Agilent), from 190 to 1100 nm.

The as-synthesized nanoparticles were characterized regarding size and morphology by transmission electron microscopy (TEM), performed with an electronic microscopy JEM-2100-JEOL. The surface charge was investigated by zeta potential analysis in a Zetasizer Nano S90 equipment, Malvern Panalytical. Experiments of temperature change *versus* irradiation time were performed to characterize the local increase in temperature induced by the photoactivation of AuNPs and AuSHINs in ultrapure water and in DMEM F12 cell culture media. 300 µL of each colloidal suspension were placed in a 96-well plate, previously coupled to a thermo sensor, and irradiated with a LED system (525 nm; 32.26 mW/cm^2).

Singlet oxygen ($^1O_2$) generation was evaluated by an indirect method using 1,3-diphenylisobenzofuran (DBPF). The reaction of DPBF with $^1O_2$ is irreversible, leading to a reduction in the absorption band of DPBF at 410 nm.[22,23] 40 µL of DBPF stock solution in acetonitrile (8 mmol/L) were mixed with 2 mL of AuSHINs in acetonitrile. To ensure comparability, all solutions were prepared to exhibit identical absorbance values at 525 nm. The experimental procedures were performed by illuminating the solutions at 525 nm (LED source, 32.26 mW/cm^2) and absorption spectra were acquired every 10 seconds of irradiation.

2.2. In vitro cell culture and lipid extraction from BT-474 human carcinoma cells

Ductal mammary carcinoma cells (BT-474) were purchased from Banco de Células do Rio de Janeiro (BCRJ ref. 0353) and cultivated in T-flasks of 25 cm^2 (Corning ref. 3290) with DMEM F12 (Sigma ref. D8900-10X1L) supplemented with 10% of fetal bovine serum (FBS, Cultilab ref. 0521-500), antibiotics and antimycotics (ThermoFisher, ref. 15240-062) at 37ºC and 5% of CO_2. The cells were cultured by replacing the DMEM F12 media every 48 hours and passaging them once a week upon reaching a confluency of at least 80%. The cells were washed with 5 mL of phosphate buffered saline (PBS), detached from the T-flask using 0.5 mL of trypsin, and subsequently seeded in a 96-well plate for 24 hours to attain a confluency of ≥ 80%. The remaining harvested cells were transferred to a new T-flask with fresh media to continue cultivation. The 2.2 x 10^{12}, 5.5 x 10^{12} and 2.2 x 10^{13} AuSHINs/mL concentrations were prepared in DMEM F12 and incubated with the BT-474 cells seeded in the 96-well plate, obtaining a final volume of 100 µL/well. The cell culture was irradiated for 1 h at 525 nm and 32.26 mW/cm^2, using a LED system (BioLambda) coupled to a digital controller. Non-irradiated cells in DMEM F12 (without AuSHINs) were considered 100% viable and used as cellular control, while irradiated cells in DMEM F12 (without AuSHINs) were established as irradiated cellular control.

Lipid extracts from BT-474 were obtained by harvesting and transferring the cells from the T-flasks to centrifugation microtubes. A cellular pellet was formed upon centrifugation (500g for 5 min), the supernatant was replaced by 1 mL of ultrapure, succeeded by 10 min of stirring. After cell lysis, 4 mL of chloroform were added with further 1 h sonication. This process resulted in two different phases: a water-soluble phase, containing cell fragments that are soluble in water, and a water-insoluble phase with cell fragments that have affinity to chloroform, which is enriched with lipids derived from BT-474 cells. The water-soluble phase was removed, and the lipid extracts from BT-474 cells were transferred to appropriated amber vials for further production of the Langmuir and Langmuir-Schaefer (LS) films.[9,17]

2.3. Langmuir and Langmuir-Schaefer (LS) films

Nanostructured films of BT-474 were produced in a Langmuir trough (KSV-NIMA model KN 2001 and 2002), by spreading the cell lipid extract (chloroform solution) on PBS and AuSHINs-PBS subphase (final concentration = 5.5 x 10^{12}

AuSHINs/mL), simulating the pH of the cellular environment. The chloroform from the cell lipid extract solution was left to evaporate for 10 min at air/subphase interface, followed by further symmetrical barrier compression (5 mm/min). Then, isotherms that correlates surface pressure (π) with area (A; cm²/mL of cell lipid extract) were acquired by a Wilhelmy (Pt) sensor at room temperature (23°C). Triplicates of every experiment were performed with a maximum dispersion of 2 mN/m, ensuring the reproducibility of the isotherm data. Information regarding the surface compression modulus (C_s^{-1}) was accessed from the isotherms, applying the equation $C_S^{-1} = -A\left(\frac{d\pi}{dA}\right)$, where C_s^{-1} is the surface compression modulus or in-plane elasticity, A is the area occupied by the film and π is the surface pressure, at a given temperature.[24,25] Additionally, surface area experiments were carried out by maintaining the surface pressure at 30 mN/m, and monitoring the area modifications over time, for non-irradiated and irradiated Langmuir films. The choice of 30 mN/m was based on the understanding that this value corresponds to the lateral pressure observed in cell membranes.[13] In the latter, the setup was assembled by irradiating the film using a green LED (530 nm, 50 W/BRIWAX FFG) positioned 20 cm on the top of the film interface, ensuring a uniform radiance.

Langmuir-Schaefer (LS) films of BT-474 lipid extract and BT-474 lipid extract + AuSHINs were built up by transferring the Langmuir films on PBS subphase and on AuSHINs-PBS subphase to solid substrates at 30 mN/m. The LS depositions were done in a horizontally approach at air/subphase interface with subsequently lifted-off cycles.[9,17,26,27] The film growth was tracked by UV-Vis absorption spectroscopy (Agilent spectrometer, Cary 60, from 190 to 800 nm) measurements of the LS multilayers onto quartz substrates. The molecular interaction between BT-474 lipid extract and AuSHINs was investigated by Fourier-transform infrared spectroscopy (FTIR). For that, LS films were deposited on germanium substrates and FTIR spectra were taken using a Bruker spectrometer with 4 cm^{-1} spectral resolution and 256 scans (Alpha II, Billerica, MA, USA) at transmission mode.

2.4. BT-474 in vitro analysis

Morphological changes induced by the AuSHINs adsorption, as well as the PTT effects on BT-474 cells, were accessed by confocal fluorescence microscopy (Nikon C2/C2si Eclipse Ti-E, Kyoto, Japan, equipped with 40x air objective - NA 0.9 - and lasers at 405 and 488 nm). The confocal images, along with the measurement of nuclei size,

average value, and standard deviation, were analyzed and quantified using ImageJ®. The cells were seeded in a 24 well-plate, containing glass coverslips underneath, and cultured for 24 hours until they reached a confluency of at least 80%. The 2.2 x 10^{12}, 5.5 x 10^{12} and 2.2 x 10^{13} AuSHINs/mL concentrations were incubated with the cell culture for 6 h, succeeded by 1 h of irradiation. After incubation and irradiation, the BT-474 cells received the membrane labeler WGA Alexa Fluor ® 488 conjugate (Invitrogen, Gaithersburg, MD, USA, ref. W11261, 5.0 × 10^{-6} g/mL, exc. 495 nm and em. 519 nm) for 10 min. The wells were subsequently rinsed with PBS for at least 5 times. Subsequently, the coverslips were detached and assembled onto glass slides using ProLong™ Gold (ref. P36931; Molecular Probes, Eugene, OR, USA) containing DAPI (4,6- diamidino-2-phenylindole; Invitrogen, Gaithersburg, MD, USA, ref. R37606, exc. 358 nm and em. 455 nm) for nuclei staining. The samples were left to dry for 24 h, sealed, and stored in the fridge.

Membrane integrity of the BT-474 cells incubated for 2 h with the three concentrations of AuSHINs and subsequent irradiation was evaluated by lactate dehydrogenase (LDH) assay.[9] LDH is commonly found in the cytoplasm and can be leakage upon cell membrane damage. LDH can be quantified by a coupled enzymatic reaction in which LDH catalyzes the conversion of lactate to pyruvate via reduction of NAD+ to NADH. The oxidation of NADH by diaphorase leads to the reduction of the tetrazolium salt (iodonitrotetrazolium; INT) to formazan, which can be measured spectrophotometrically at 450 nm. The level of formazan is directly proportional to the amount of LDH released, which is indicative of the cell membrane damage.[28] The LDH release (%) was calculated by using the manufacturer recommendations (CyQUANT™ LDH Cytotoxicity Assay Kit. Catalog Numbers C20300 and C20301. Pub. No. MAN0018500). Experimental data were plotted with GraphPad Prism® 8 and estimated by analysis of variance (one unpaired multiple t-test), followed by Bonferroni test ($P \leq 0.05$), ensuring measurements in triplicate. Figure 1 depicts a schematic representation of the experimental procedures conducted in this study, including the synthesis of AuSHINs, fabrication of Langmuir and LS films, and subsequent *in vitro* assays.

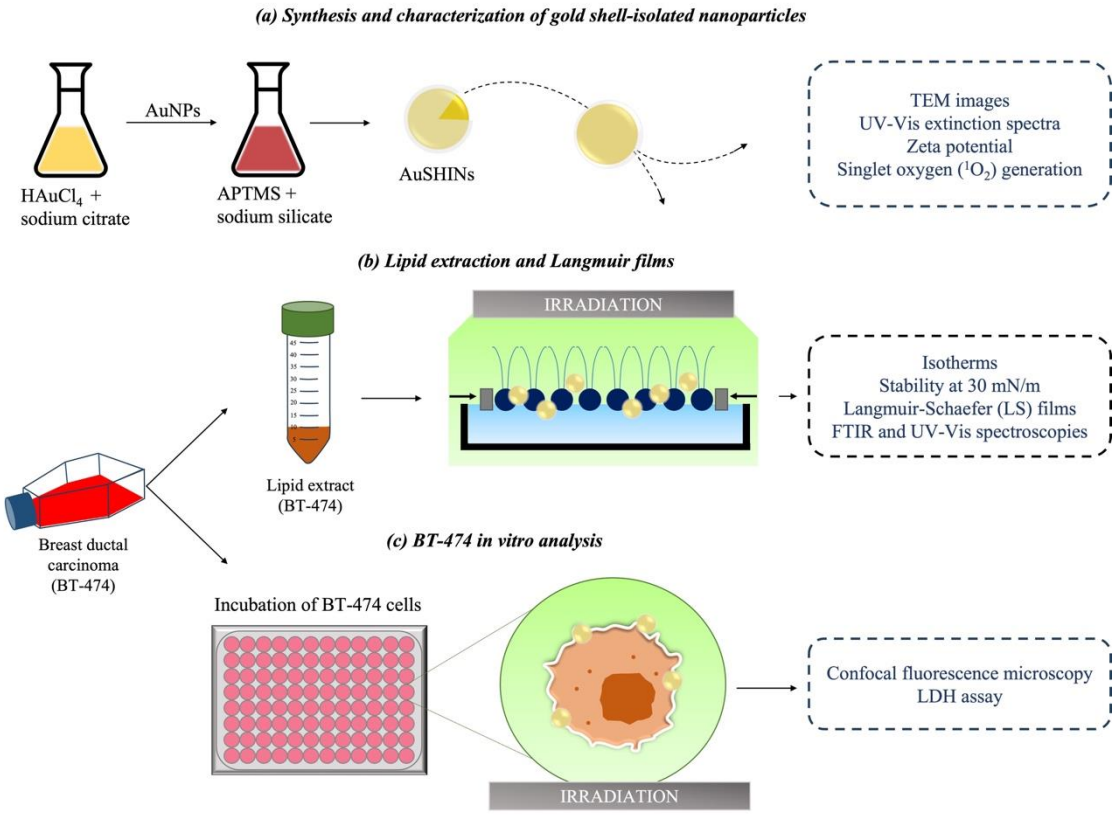

Figure 1. Schematic representation of the experimental procedures for (a) synthesis and characterization of AuNPs and AuSHINs, (b) lipid extraction, fabrication and characterization of Langmuir and LS films, and (c) *in vitro* assays.

3. Results and Discussion

3.1. AuSHINs characterization

The core and silica shell sizes of gold nanoparticles (AuNPs) and gold shell-isolated nanoparticles (AuSHINs) were estimated via histograms built from TEM images (Figure S1a and S1b, Supplementary Material). The gold cores presented 13.0 ± 1.4 nm of diameter and the silica shells 5.5 ± 1.0 nm of thickness, which are comparable to the reported in the literature.[9,12,29] UV-Vis extinction spectra and zeta potential of the nanoparticles diluted in ultrapure water and in culture media (DMEM F12) are exhibited in Figure 2a and 2b. In ultrapure water, the localized surface plasmon resonance (LSPR) at 518 nm for AuNPs is displaced to 525 nm for AuSHINs owing to the change in the refractive index induced by the silica coating.[30–32] When negatively charged AuNPs are exposed to DMEM F12, cations present in the media neutralize the citrate groups of the nanoparticles, disrupting the electrostatic repulsions responsible for maintaining the colloidal stability, along with the van der Waals interactions.[33,34] Such effect leads to the AuNP aggregation, which is confirmed by the widening of the plasmon (Figure 2a)

towards 672 nm[35] and the increase of the zeta potential from - 38.5 mV to - 11.6 mV (Figure 2b). Comparable increment in the zeta potential was observed for AuNPs with 10 to 13 nm in saline media ($NaNO_3$ 0.025 mol/L).[34] On the other hand, the silica coating of AuSHINs prevented changes in the UV-Vis spectral profile when in presence of DMEM F12 (Figure 2a), suggesting non-aggregation of the nanostructures. Besides, the zeta potential in DMEM F12 (- 23.7 mV) is similar to that found in ultrapure water (- 28.2 mV), indicating that the ions present in DMEM F12 did not affect the charge stability of AuSHINs.

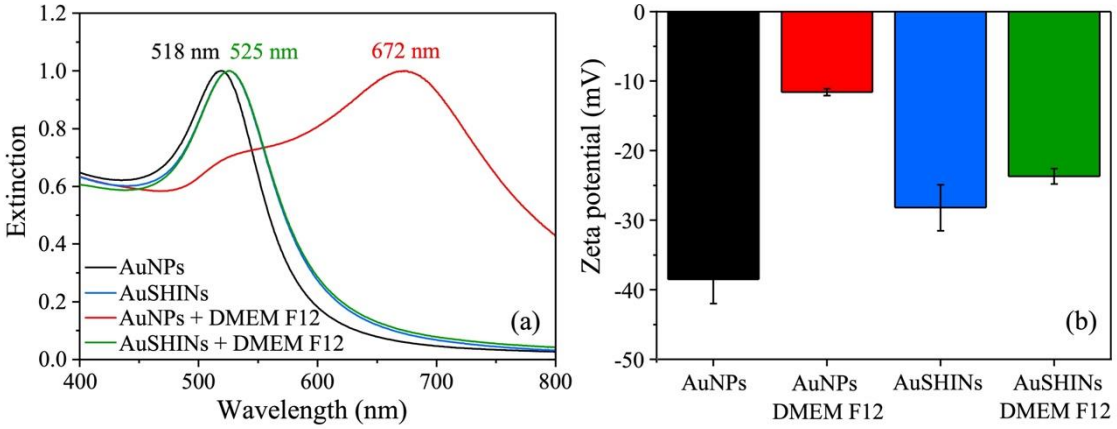

Figure 2. (a) UV-Vis extinction spectra and (b) zeta potential for AuNPs and AuSHINs diluted (1:1 v/v) in ultrapure water and DMEM F12 culture media.

The local increase in temperature over the irradiation time was measured for AuNPs and AuSHINs in ultrapure water and in DMEM F12 (Figure S1c), using a LED source (525 nm; 32.26 mW/cm^2) in full resonance with the LSPR. The overall photoinduced heating by AuSHINs has shown to be higher than that by AuNPs, independent of the media. Although the rise in temperature for AuSHINs in ultrapure water (~14°C) was slightly higher than in DMEM F12 (~12.5 °C), the silica coating did not affect the conversion of light into heat. In fact, compared to others gold nanostructures, the light dose required by the AuSHINs to generate similar increment in temperature is lower than for nanoprisms,[36] gold-decorated silicon nanopillars,[37] PEGylated nanocages,[38] and even for PEGylated spherical nanoparticles,[39] highlighting the potential of AuSHINs for *in vitro* and *in vivo* applications. Table 1 summarizes the mentioned doses of light reported for different nanostructures to produce the same temperature rise.

Table 1. Light doses required for different nanostructures to produce similar increase in temperature.

Nanostructure	Temperature change	Light dose
Gold nanoprisms[36]	12 °C in culture media	3000 J/cm^2
Gold-decorated silicon nanopillars[37]	12 °C in PBS solution	375 J/cm^2
PEG-gold nanocages[38]	12 °C in culture media	720 J/cm^2
PEG-gold nanoparticles[39]	12 °C in culture media	206.4 J/cm^2
Current AuSHINs	12.5 °C in culture media	129 J/cm^2

3.2. AuSHINs incorporation into BT-474 lipid membrane and photoinduced effects

Figure 3a shows π-A isotherms of BT-474 lipid extract on PBS and AuSHINs subphases. The incorporation of AuSHINs expanded the BT-474 monolayers, causing a ca. 12.5% isotherm shift towards higher mean areas. The monolayer collapse slightly increased from 44 to 47 mN/m, although the isotherm profile remained unchanged. Larger displacements were induced by AuSHINs on both pulmonary A549 (39%) and mammary MCF-7 (39%) lipid extract isotherms, suggesting a smaller adsorption of AuSHINs into BT-474 membrane.[9] The surface compression modulus (C_S^{-1}) in Figure 3b shows that the BT-474 monolayers are in the fluid phase and that the incorporation of AuSHINs increases the membrane flexibility at 30 mN/m, since C_S^{-1} decreased from 35 to 30 mN/m. The C_S^{-1} modifications are important as they can impact the charge and mass transport across the membrane, which is consistent with previously reported data on A549 and MCF-7 lipid extract monolayers.[9] Conversely, incorporation of AuNPs and AuNPs-ALA into neat DPPC and DPPS lipid monolayers led to an increase in C_S^{-1}, resulting in more rigid membranes.[40,41] Such differences might be related to the complexity of the BT-474 lipid extract, as evidenced by its inherent fluidity on PBS subphase in comparison to the liquid-expanded and liquid-condensed phases observed for neat DPPC and DPPS monolayers on ultrapure water.

Molecular-level interactions between BT-474 lipid extract and AuSHINs were accessed here by Fourier-transform infrared spectroscopy (FTIR) of Langmuir-Schaefer (LS) films. Multilayers of BT-474 lipid extract on PBS and on AuSHINs subphases were transferred to solid substrates, controlled by UV-Vis absorption spectroscopy (Figure S2). The vibrational modes of the head and lipid chain groups of the LS films are presented in

the FTIR spectra shown in Figures 3c and 3d, respectively, with the assignments provided in Table 2. FTIR spectrum of the AuSHINs drop-cast film is given in Figures 3c and 3d as reference. The AuSHINs insertion into the BT-474 LS films induced stronger modifications in the head region of the spectrum, specially related to the υ(C-O) band from AuSHINs. For instance, the $\upsilon_s(PO_2^-)$ and υ_{as}(C-O-C) of the lipid extract at 1090 cm^{-1} and 1163 cm^{-1} overlap with the υ(C-O) of the AuSHINs at 1108 cm^{-1}. Furthermore, the υ(C-O) shifted toward higher wavenumbers when compared to the AuSHINs drop-cast spectrum (from 1101 to 1108 cm^{-1}). Such changes might indicate that the C-O group from AuSHINs plays an important role in the interaction mechanism with BT-474 lipid extract. Meanwhile, the $\upsilon_{as}(PO_2^-)$ shifted from 1241 to 1221 cm^{-1}, indicating the presence of H-bonds between PO_2^- groups in the BT-474 + AuSHINs LS film. Since the zeta potential of AuSHINs (- 28.2 mV in ultrapure water) is negative, electrostatic interactions with anionic phosphates are expected and may also affect their vibrational modes. The $\delta(CH_2)$ shifted from 1460 to 1464 cm^{-1} and the υ(C=O) at 1738 cm^{-1} had a drastic decrease owing to the reorientation of the carbonyl groups interacting with AuSHINs.

Regarding the lipid chain groups, the $\upsilon_{as}(CH_3)$ shifted from 2958 to 2953 cm^{-1} and the intensity ratio of the CH_2 vibrational modes (I_{as}/I_s) increased from 1.02 to 1.17, meaning a reduction in the conformational order of the aliphatic tails.[42,43] Therefore, it is likely that the AuSHINs have been driven to the BT-474 monolayers mainly by electrostatic interactions, limiting their insertion into the head groups, until the carbonyl region. The reorganization of head groups upon AuSHINs interaction may have led to disorganization of lipid chains, similarly to what was previously observed for MCF-7 lipid extract.[9]

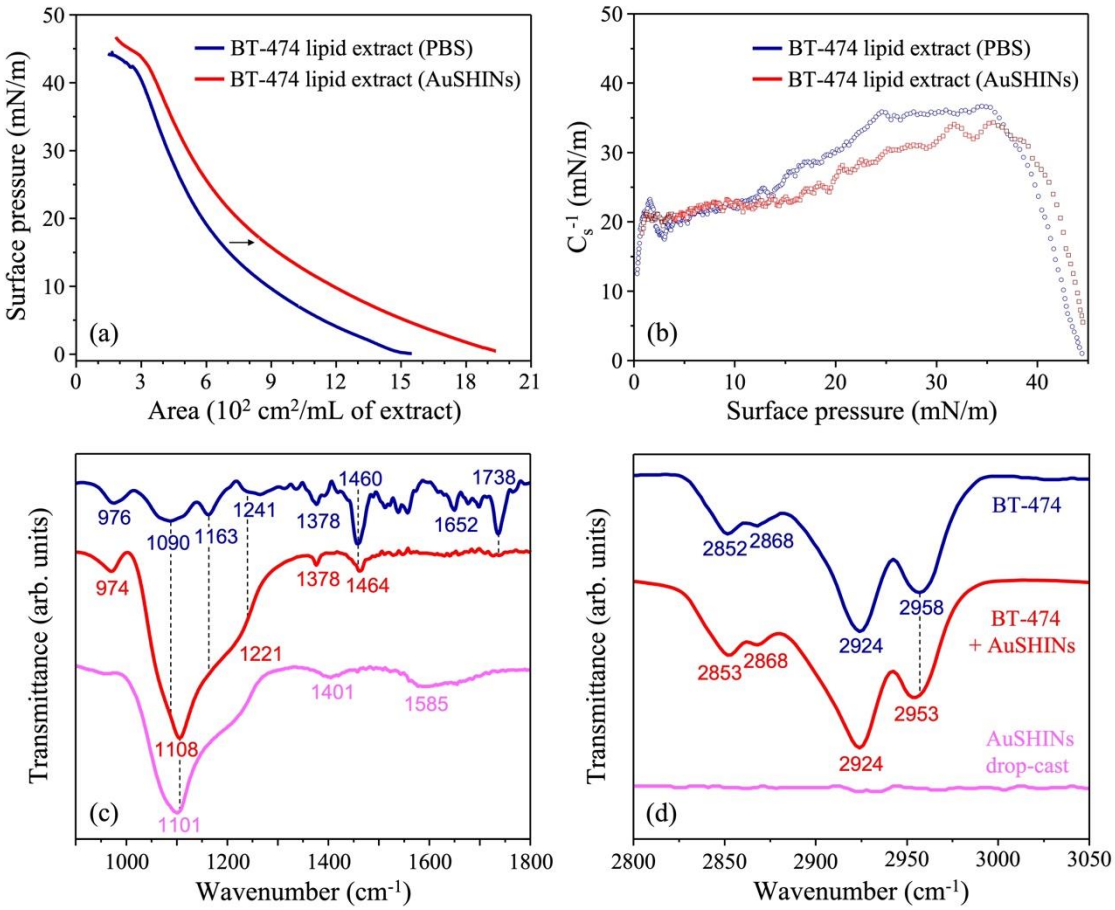

Figure 3. (a) π-A isotherms and (b) surface compression modulus (C_S^{-1}) of BT-474 lipid extract membrane on PBS (blue) and AuSHINs (red) subphases. AuSHINs lack surface activity and do not produce isotherms. FTIR spectra of BT-474, BT-474 + AuSHINs LS films (40 depositions) and AuSHINs drop-cast on Ge substrates. The spectra were categorized into the vibrational modes of the (c) head and (d) lipid chain regions.

Table 2. Main vibrational mode assignments in FTIR spectra of BT-474 and BT-474 + AuSHINs LS films, besides AuSHINs drop-cast film.

Assignments	LS film (cm^{-1})		Drop-cast film (cm^{-1})
	BT-474	BT-474 + AuSHINs	AuSHINs
$\upsilon_{as}(CH_3)$ [43,44]	2958	**2953**	-
$\upsilon_{as}(CH_2)$ [43–45]	2924	2924	-
$\upsilon_{s}(CH_3)$ [43–45]	2868	2869	-
$\upsilon_{s}(CH_2)$ [43–45]	2852	2853	-
$\upsilon(C=O)$ [45,46]	1738	1738	-
$\delta(H_2O)$ [46]	1652	-	-

$\upsilon_{as}(COO^-)$ [47]	-	-	1585
$\delta(CH_2)$ [44,46,48]	1460	**1464**	1401
$\upsilon(CH_2)$ [46]	1378	1378	-
$\upsilon_{as}(PO_2^-)$ [44,49]	1241	**1221**	-
υ_{as}(C-O-C) [45,50]	1163	-	-
υ(C-O) [47]	-	**1108**	1101
$\upsilon_s(PO_2^-)$ [46,49]	1090	-	-
$\upsilon_{as}(CN^+(CH_3)_3)$ [44,46]	976	974	-

*Significant band shifts were defined as variations ≥ 4 cm^{-1}, in accordance with FTIR spectral resolution.

The photoinduced effects triggered by AuSHINs were evaluated by comparing the relative areas of irradiated and non-irradiated BT-474 monolayers, at constant surface pressure of 30 mN/m. Light-irradiation caused no significant modification in BT-474 monolayers on PBS, as shown in Figure 4a. The decrease in relative area over time is ascribed to the unregulated lipid oxidation caused by reactive oxygen species (ROS) from the environment,[51] which results in the loss of material to the subphase. Upon AuSHINs incorporation (Figure 4b), irradiated BT-474 monolayer became less unstable, presenting a relative area of ca. 2.0 % (from 90.4% ± 0.8% to 92.3% ± 0.9%) larger than the non-irradiated monolayer. AuSHINs sustain LSPR upon visible irradiation and the collective oscillation of electrons generates localized heating, which may have impacted the stability of the monolayers. Moreover, photoexcited AuSHINs can transfer electrons and/or energy to molecular oxygens (O_2) generating ROS, such as singlet oxygen ($^1O_2$) and free radicals. According to the literature, the mechanism is similar to that reported for type I and type II mechanisms of the photosensitizers used in photodynamic therapy (PDT).[22,52] ROS generated near the cell membrane can trigger a variety of photochemical reactions, especially in unsaturated phospholipids.[18,53–56] As example, hydroperoxides can be formed at the unsaturation sites of the carbon tails (Figure 4c), disrupting the hydrophilic-hydrophobic equilibrium within the membrane, which may explain the overall surface area increase of BT-474 irradiated monolayers (Figure 4b).[57] Indeed, the generation of $^1O_2$ was detected here using an indirect method, wherein AuSHINs were irradiated in the presence of a 1,3-diphenylisobenzofuran (DPBF) probe (Figure 4d) using a LED source

at 525 nm (32.26 mW/cm^2). The decay in the DPBF absorption band at 410 nm over the 120-second irradiation period was considerably more significant than the decrease in the extinction band of AuSHINs, indicating a progressive increase in the concentration of $^1O_2$ generated upon irradiation.

Lipid extract monolayers of MCF-7 also presented a surface area increase when irradiated on AuSHINs subphase.[9] The main reaction at the lipid chains was proposed to be hydroperoxidation, resulting from the constrained AuSHINs incorporation into the film. The similarity of the photochemical effects observed on MCF-7 and BT-474 lipid extract monolayers might be explained by the analogous lipid composition, since both are human breast cancer cells and share important characteristics. For instance, both cell lines have comparable lipid contents, in which phosphatidylcholines (PC) and phosphatidylethanolamines (PE) were found to be the most abundant phospholipids, while sphingomyelin (SM) was the most abundant sphingolipid.[58] Additionally, both cell lines have similar profiles of fatty acids, in which oleic acid (C18:1) is the most abundant, followed by palmitic acid (C16:0) and stearic acid (C18:0).[59] In fact, the lipid composition of membranes plays an important role on the photochemical outcomes. So much that an opposite effect was noticed for lipid extract monolayers of A549 on AuSHINs subphase, which is a cancer cell line from lung adenocarcinoma. The deep insertion of AuSHINs into A549 membrane led to the cleavage of the lipid chains.[9]

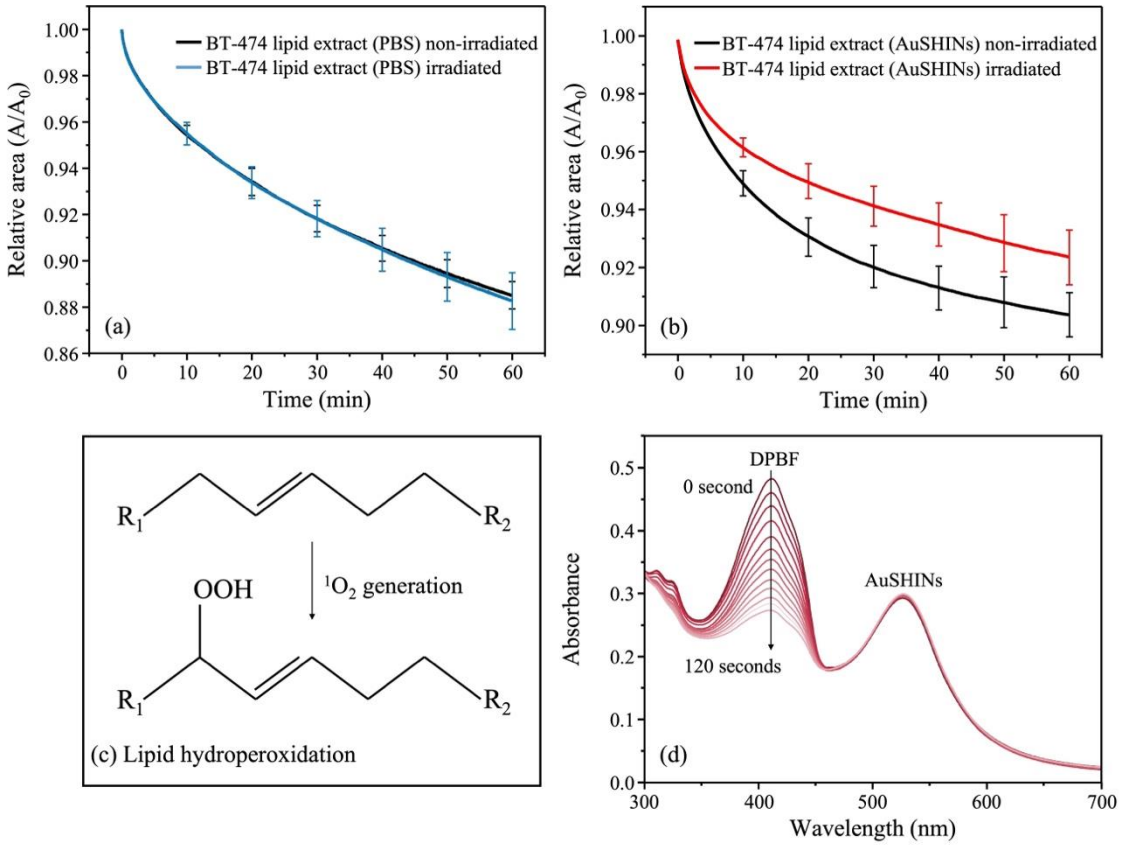

Figure 4. Changes in relative area of irradiated and non-irradiated BT-474 lipid extract monolayers on (a) PBS and (b) AuSHINs subphases. A_0 is the initial area extrapolated for BT-474 lipid extract membrane at 30 mN/m. (c) Schematic representation of hydroperoxidation occurring at the unsaturation sites of lipid chains. (d) Absorption spectra of AuSHINs (2.2 x 10^{12} AuSHINs/mL) mixed with DPBF and acquired every 10 seconds upon irradiation with 525 nm LED source (32.26 mW/cm^2).

3.3. In vitro BT-474 cell assays

The photoinduced effects by AuSHINs were also evaluated on *in vitro* systems based on BT-474 cells. The impact of the AuSHINs incorporation and further photoinduced effects on BT-474 cell membranes and nuclei were determined by confocal fluorescence microscopy, as shown in Figure 5. BT-474 cells were incubated for 6 h with AuSHINs at 2.2 x 10^{12}, 5.5 x 10^{12} and 2.2 x 10^{13} NPs/mL before (non-irradiated) and after photoactivation (irradiated). The non-irradiated cellular control (Figure 5a) and cells incubated with the lowest AuSHINs concentration (Figure 5b), exhibit well defined nuclei and membranes, indicating that the morphological integrity of the cells was preserved. Slight modifications in the membrane labelling are observed at higher AuSHINs concentrations (Figure 5c and 5d), corroborating with the low internalization process reported for non-functionalized nanoparticles incubated with BT-474.[60] Irradiated

cellular control (Figure 5e) also preserved the morphological integrity, with no significant differences from non-irradiated control (Figure 5a). However, after AuSHINs photoactivation (Figure 5f, 5g and 5h), the cellular membrane is fragmented, and the nuclei seem to reduce in size. Similarly, irradiated PEG-gold nanoparticles induced membrane disintegration in a cell line of mammary ductal carcinoma (Hs 578T), even when applied low doses of light (14 W/cm^2).[61] Regarding the nuclei dimensions, there were no statistically significant changes for non-irradiated cells, independently of AuSHINs concentration. Although a decrease in nuclei diameter might be recognized after AuSHINs photoactivation (Figure S3), the statistical difference is only ascertained for the BT-474 cells incubated with the highest concentration of 2.2 x 10^{13} AuSHINs/mL.

The externalization of the cytosolic lactate dehydrogenase (LDH) to the culture media was quantified in irradiated and non-irradiated BT-474 cells incubated with 2.2 x 10^{12}, 5.5 x 10^{12} and 2.2 x 10^{13} AuSHINs/mL concentrations, as shown in Figure 6. LDH assay measures the percentage of LDH released owing to the damage in the cell membrane integrity. Higher LDH percentage indicates higher level of plasma membrane disruption and, consequently, more cellular death. The LDH level increases with the AuSHINs concentration, independent of the condition (under photoactivation or not). For instance, the LDH release for non-irradiated cells increases from 10 to 43% at 2.2 x 10^{12} and 2.2 x 10^{13} AuSHINs/mL, respectively. Upon photoactivation, the same AuSHINs concentrations led to 45 and 80% of LDH release, respectively. Therefore, one may assume that AuSHINs incorporation induces modifications in plasma membrane that are intensified upon irradiation, revealing an increase in cell mortality owing to severe damages to the cell permeability. Indeed, the death rate of tumoral cells using photoactivated AuSHINs has demonstrated to be higher than similar systems.[62–64] For instance, Au-Ag nanostructures containing aptamers were not able to trigger MCF-7 cell death after 30 min of incubation followed by 1 h of irradiation at 0.06 W/cm^2. Even when applying greater irradiances, the cell mortality was still lower, achieving 25 and 46% of cell death at 0.13 and 0.19 W/cm^2 of irradiance, respectively.[64]

Combining the nuclei modification and the cell membrane fragmentation, noticed via confocal microscopy, with the LDH outcome, one may suggest necrosis as one of the possible cell death mechanisms. Cells exposed to heat often activate the necrotic pathway,[65] exhibiting cellular swelling, early loss of plasma membrane integrity, influx of extracellular ions and fluid, resulting in cellular and organelle edema, and nuclear alterations such as pyknosis.[66,67] However, apoptosis cannot be ruled out completely, as

changes in cellular nuclei may also occur during the apoptotic pathway of cell death.[68,69] Indeed, the outcome of PTT can vary and trigger different death pathways, including early apoptosis, late apoptosis, or necrosis. This depends on various factors, such as the light dose, photothermal properties of the nanomaterial, concentration of nanoparticles, incubation period, irradiation conditions, amongst others, as described by Riley et al.[70] For instance, Gao et al.[52] observed a transition in the death pathway of Hela cells from apoptosis to necrosis by adjusting the applied dose of light, when using gold nanocages (AuNCs).

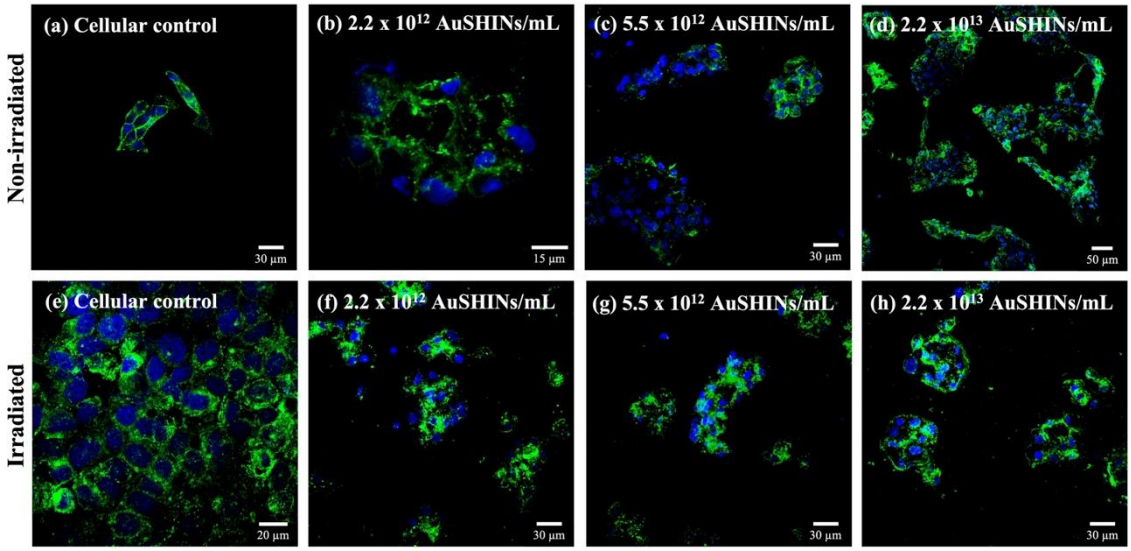

Figure 5. Confocal microscopies of the non-irradiated (a-d) and irradiated (e-h) BT-474 cells incubated for 6 h with 2.2 x 10^{12}, 5.5 x 10^{12} and 2.2 x 10^{13} AuSHINs/mL concentrations. Irradiation was carried out at 525 nm with 32.26 mW/cm^2 of irradiance. The cell nuclei were labelled with DAPI (in blue), while the cell membranes were tagged with WGA (in green).

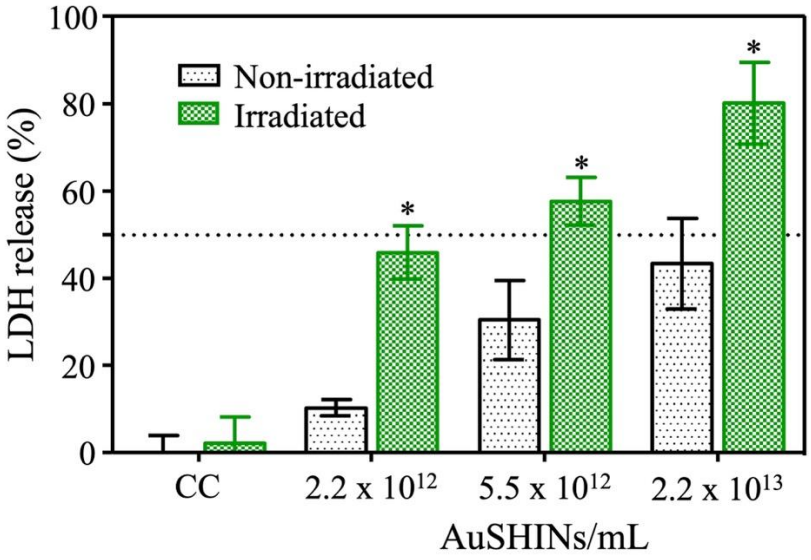

Figure 6. LDH assay for non-irradiated and irradiated BT-474 cells incubated with 2.2 x 10^{12}, 5.5 x 10^{12} and 2.2 x 10^{13} AuSHINs/mL concentrations. Irradiation was carried out at 525 nm with 32.26 mW/cm^2 of irradiance.

4. Conclusion

Using Langmuir and Langmuir-Schaefer (LS) films, we built here bioinspired plasma membranes with lipid extracts from BT-474 cells to determine the mechanisms underlying the photothermal efficiency of gold shell-isolated nanoparticles (AuSHINs). The incorporation of AuSHINs into BT-474 monolayers caused an expansion of the membrane, as evidenced by a ca. 12.5% isotherm shift towards higher mean areas and increased the membrane flexibility. The overlap of $\upsilon_s(PO_2^-)$ and υ_{as}(C-O-C) FTIR bands of the lipid extract with the υ(C-O) of AuSHINs suggests that the C-O group from AuSHINs plays an important role in the interaction mechanism with BT-474 lipid membrane, driven mainly by electrostatic interactions. AuSHINs insertion were limited to the head groups until the carbonyl region, which may have led to the disorganization of lipid chains. Upon AuSHINs incorporation, the irradiated BT-474 monolayer became less unstable, and the surface area increased by ca. 2.0% relative to the non-irradiated monolayer. Hydroperoxidation reactions at the unsaturated sites of the carbon tails affected the hydrophilic-hydrophobic equilibrium within the membrane, explaining the overall surface area increase of irradiated monolayers. The *in vitro* assays on BT-474 confirmed that oxidative reactions had an impact on the plasma membrane, leading to modifications and disruption. Furthermore, an increase in the concentration of irradiated AuSHINs resulted in a decrease in nucleus diameter, indicating a dependence of photothermal efficiency on nanoparticle concentration. In summary, these findings provide insights into the molecular-level mechanisms photoinduced by AuSHINs on BT-474 lipid membranes, which has significant implications for the photothermal therapy of ductal mammary carcinoma cells.

Acknowledgments

This work was supported by Sao Paulo Research Foundation (FAPESP 2018/16713-0, 2018/22214-6, 2022/02189-2, EMU 14/11408-3 and EMU 17/03879-4), INEO and National Council for Scientific and Technological Development (CNPq). We thank the LME - Laboratório de Microscopia Eletrônica from IQSC-USP for the TEM images. M.B.K., S.A.C., and L.G.M. are thankful for their fellowship provided by FAPESP (2021/14500-1, 2018/14692-5, 2020/15854-9, respectively).

CONFLICTS OF INTEREST

There are no conflicts to declare.

References

1. Dheyab, M. A. *et al.* Gold nanoparticles-based photothermal therapy for breast cancer. *Photodiagnosis Photodyn. Ther.* **42**, 103312 (2023).
2. Sung, H. *et al.* Global Cancer Statistics 2020: GLOBOCAN Estimates of Incidence and Mortality Worldwide for 36 Cancers in 185 Countries. *CA. Cancer J. Clin.* **71**, 209–249 (2021).
3. Kadkhoda, J. *et al.* Aptamer-conjugated gold nanoparticles for targeted paclitaxel delivery and photothermal therapy in breast cancer. *J. Drug Deliv. Sci. Technol.* **67**, 102954 (2022).
4. Casasent, A. K. *et al.* Learning to distinguish progressive and non-progressive ductal carcinoma in situ. *Nat. Rev. Cancer* **22**, 663–678 (2022).
5. Kubo, A. *et al.* Polysulfide Serves as a Hallmark of Desmoplastic Reaction to Differentially Diagnose Ductal Carcinoma In Situ and Invasive Breast Cancer by SERS Imaging. *Antioxidants* **12**, 240 (2023).
6. Park, K. W. *et al.* Ductal carcinoma in situ: a risk prediction model for the underestimation of invasive breast cancer. *npj Breast Cancer* **8**, 8 (2022).
7. Alamdari, S. G. *et al.* Recent advances in nanoparticle-based photothermal therapy for breast cancer. *J. Control. Release* **349**, 269–303 (2022).
8. Yang, K. *et al.* Low temperature photothermal therapy: Advances and perspectives. *Coord. Chem. Rev.* **454**, 214330 (2022).
9. Camacho, S. A. *et al.* The efficiency of photothermal action of gold shell-isolated nanoparticles against tumor cells depends on membrane interactions. *Colloids Surfaces B Biointerfaces* **211**, (2022).
10. Taylor, M. L., Wilson, R. E., Amrhein, K. D. & Huang, X. Gold Nanorod-Assisted Photothermal Therapy and Improvement Strategies. *Bioengineering* **9**, 200 (2022).
11. Yang, W., Liang, H., Ma, S., Wang, D. & Huang, J. Gold nanoparticle based photothermal therapy : Development and application for effective cancer treatment. *Sustain. Mater. Technol.* **22**, e00109 (2019).
12. Camacho, S. A. *et al.* Colloids and Surfaces B : Biointerfaces Molecular-level effects on cell membrane models to explain the phototoxicity of gold shell-isolated nanoparticles to cancer cells. *Colloids Surfaces B Biointerfaces* **194**, (2020).
13. Oliveira, O. N., Caseli, L. & Ariga, K. The Past and the Future of Langmuir and Langmuir-Blodgett Films. *Chemical Reviews* (2022) doi:10.1021/acs.chemrev.1c00754.
14. Geraldo, V. P. N., Pavinatto, F. J., Nobre, T. M., Caseli, L. & Oliveira, O. N. Langmuir films containing ibuprofen and phospholipids. *Chem. Phys. Lett.* (2013) doi:10.1016/j.cplett.2012.12.064.
15. Maximino, M. D., Constantino, C. J. L., Oliveira, O. N. & Alessio, P. Synergy in the interaction of amoxicillin and methylene blue with dipalmitoyl phosphatidyl choline (DPPC) monolayers. *Appl. Surf. Sci.* (2019) doi:10.1016/j.apsusc.2019.01.065.
16. Sakai, A. *et al.* The lipid composition affects Trastuzumab adsorption at monolayers at the air-water interface. *Chem. Phys. Lipids* (2020) doi:10.1016/j.chemphyslip.2020.104875.
17. Bistaffa, M. J. *et al.* Plasma membrane permeabilization to explain erythrosine B phototoxicity on in vitro breast cancer cell models. *J. Photochem. Photobiol. B*

Biol. (2021) doi:10.1016/j.jphotobiol.2021.112297.
18. Pereira, L. S. A. *et al.* Mechanisms of hypericin incorporation to explain the photooxidation outcomes in phospholipid biomembrane models. *Chem. Phys. Lipids* (2022) doi:10.1016/j.chemphyslip.2022.105181.
19. Villanueva, M. E., Lanterna, A. E. & Vico, R. V. Hydrophobic silver nanoparticles interacting with phospholipids and stratum corneum mimic membranes in Langmuir monolayers. *J. Colloid Interface Sci.* (2019) doi:10.1016/j.jcis.2019.02.069.
20. Grabar, K. C., Freeman, R. G., Hommer, M. B. & Natan, M. J. Preparation and characterization of Au colloid monolayers. *Anal. Chem.* **67**, 735–743 (1995).
21. Aroca, R. F. *et al.* Plasmon-Enhanced Fluorescence and Spectral Modification in SHINEF. *J. Phys. Chem. C* **115**, 20419–20424 (2011).
22. Pasparakis, G. Light-induced generation of singlet oxygen by naked gold nanoparticles and its implications to cancer cell phototherapy. *Small* (2013) doi:10.1002/smll.201301365.
23. Tada, D. B. & Baptista, M. S. Photosensitizing nanoparticles and the modulation of ROS generation. *Frontiers in Chemistry* (2015) doi:10.3389/fchem.2015.00033.
24. J.T. Davies; E.K. Rideal. *'Interfacial Phenomena'*. (1963).
25. Aoki, P. H. B. *et al.* Molecular-level modifications induced by photo-oxidation of lipid monolayers interacting with erythrosin. *Langmuir* **32**, 3766–3773 (2016).
26. Moreira, L. G., Almeida, A. M., Nield, T., Camacho, S. A. & Aoki, P. H. B. Modulating photochemical reactions in Langmuir monolayers of Escherichia coli lipid extract with the binding mechanisms of eosin decyl ester and toluidine blue-O photosensitizers. *J. Photochem. Photobiol. B Biol.* (2021) doi:10.1016/j.jphotobiol.2021.112173.
27. Camacho, S. A. *et al.* Supramolecular arrangements of an organometallic forming nanostructured films. in *Materials Research* (2014). doi:10.1590/1516-1439.279014.
28. Aslantürk, Ö. S. In Vitro Cytotoxicity and Cell Viability Assays: Principles, Advantages, and Disadvantages. in *Genotoxicity - A Predictable Risk to Our Actual World* (2018). doi:10.5772/intechopen.71923.
29. Camacho, S. A., Sobral-Filho, R. G., Aoki, P. H. B., Constantino, C. J. L. & Brolo, A. G. Zika Immunoassay Based on Surface-Enhanced Raman Scattering Nanoprobes. *ACS Sensors* **3**, 587–594 (2018).
30. Camacho, S. A., Sobral-Filho, R. G., Aoki, P. H. B., Constantino, C. J. L. & Brolo, A. G. Immunoassay quantification using surface-enhanced fluorescence (SEF) tags. *Analyst* **142**, 2717–2724 (2017).
31. Guerrero, A. R., Albella, P. & Aroca, R. F. Plasmon Enhanced Fluorescence with Aggregated Shell-Isolated Nanoparticles. 1–6 (2014).
32. Bistaffa, M. J. *et al.* Immunoassay platform with surface-enhanced resonance Raman scattering for detecting trace levels of SARS-CoV-2 spike protein. *Talanta* (2022) doi:10.1016/j.talanta.2022.123381.
33. Oh, E. *et al.* Colloidal stability of gold nanoparticles coated with multithiol-poly(ethylene glycol) ligands: Importance of structural constraints of the sulfur anchoring groups. *J. Phys. Chem. C* (2013) doi:10.1021/jp405265u.
34. Pamies, R. *et al.* Aggregation behaviour of gold nanoparticles in saline aqueous media. *J. Nanoparticle Res.* (2014) doi:10.1007/s11051-014-2376-4.
35. Grabar, K. C., Freeman, R. G., Hommer, M. B. & Natan, M. J. Preparation and Characterization of Au Colloid Monolayers. *Anal. Chem.* **67**, 735–743 (1995).

36. Pérez-Hernández, M. *et al.* Dissecting the Molecular Mechanism of Apoptosis during Photothermal Therapy Using Gold Nanoprisms. *ACS Nano* **9**, 52–61 (2015).
37. Alhmoud, H., Cifuentes-Rius, A., Delalat, B., Lancaster, D. G. & Voelcker, N. H. Gold-decorated porous silicon nanopillars for targeted hyperthermal treatment of bacterial infections. *ACS Appl. Mater. Interfaces* (2017) doi:10.1021/acsami.7b13278.
38. Wang, Y. *et al.* Comparison study of gold nanohexapods, nanorods, and nanocages for photothermal cancer treatment. *ACS Nano* (2013) doi:10.1021/nn304332s.
39. Mendes, R., Pedrosa, P., Lima, J. C., Fernandes, A. R. & Baptista, P. V. Photothermal enhancement of chemotherapy in breast cancer by visible irradiation of Gold Nanoparticles. *Sci. Rep.* **7**, 1–9 (2017).
40. da Silva, R. L. C. G., da Silva, H. F. O., da Silva Gasparotto, L. H. & Caseli, L. Lipopolysaccharides and peptidoglycans modulating the interaction of Au naparticles with cell membranes models at the air-water interface. *Biophys. Chem.* **238**, 22–29 (2018).
41. da Silva, R. L. C. G., de Oliveira Gonçalves, K., Courrol, L. C. & Caseli, L. Study of the interactions of gold nanoparticles functionalized with aminolevulinic acid in membrane models. *Colloids Surfaces B Biointerfaces* (2021) doi:10.1016/j.colsurfb.2021.111849.
42. Mendelsohn, R., Mao, G. & Flach, C. R. Infrared reflection-absorption spectroscopy: Principles and applications to lipid-protein interaction in Langmuir films. *Biochimica et Biophysica Acta - Biomembranes* (2010) doi:10.1016/j.bbamem.2009.11.024.
43. Dicko, A., Bourque, H. & Pézolet, M. Study by infrared spectroscopy of the conformation of dipalmitoylphosphatidylglycerol monolayers at the air-water interface and transferred on solid substrates. *Chem. Phys. Lipids* (1998) doi:10.1016/S0009-3084(98)00084-X.
44. Inan Genç, A., Gok, S., Banerjee, S. & Severcan, F. Valdecoxib Recovers the Lipid Composition, Order and Dynamics in Colon Cancer Cell Lines Independent of COX-2 Expression: An ATR-FTIR Spectroscopy Study. *Appl. Spectrosc.* (2017) doi:10.1177/0003702816654164.
45. Simsek Ozek, N., Tuna, S., Erson-Bensan, A. E. & Severcan, F. Characterization of microRNA-125b expression in MCF7 breast cancer cells by ATR-FTIR spectroscopy. in *Analyst* (2010). doi:10.1039/c0an00543f.
46. Blaudez, D. *et al.* Investigations at the air/water interface using polarization modulation IR spectroscopy. *J. Chem. Soc. - Faraday Trans.* (1996) doi:10.1039/ft9969200525.
47. Rajeshkumar, S. Anticancer activity of eco-friendly gold nanoparticles against lung and liver cancer cells. *J. Genet. Eng. Biotechnol.* (2016) doi:10.1016/j.jgeb.2016.05.007.
48. Severcan, F., Bozkurt, O., Gurbanov, R. & Gorgulu, G. FT-IR spectroscopy in diagnosis of diabetes in rat animal model. *J. Biophotonics* (2010) doi:10.1002/jbio.201000016.
49. Derenne, A., Vandersleyen, O. & Goormaghtigh, E. Lipid quantification method using FTIR spectroscopy applied on cancer cell extracts. *Biochim. Biophys. Acta - Mol. Cell Biol. Lipids* (2014) doi:10.1016/j.bbalip.2013.10.010.
50. Ferreira, J. V. N., Lago, J. H. G. & Caseli, L. Thymol in cellular membrane models formed by negative charged lipids causes aggregation at the air-water

interface. *Chem. Phys. Lett.* (2019) doi:10.1016/j.cplett.2019.01.006.
51. Liljeblad, J. F. D., Bulone, V., Tyrode, E., Rutland, M. W. & Johnson, C. M. Phospholipid monolayers probed by vibrational sum frequency spectroscopy: Instability of unsaturated phospholipids. *Biophys. J.* (2010) doi:10.1016/j.bpj.2010.02.009.
52. Gao, L. *et al.* Plasmon-Mediated Generation of Reactive Oxygen Species from Near-Infrared Light Excited Gold Nanocages for Photodynamic Therapy in Vitro. *ACS Nano* **8**, 7260–7271 (2014).
53. Yu, Z. *et al.* Reactive Oxygen Species-Related Nanoparticle Toxicity in the Biomedical Field. *Nanoscale Res. Lett.* **15**, 115 (2020).
54. Moreira, L. G. *et al.* Chain Cleavage of Bioinspired Bacterial Membranes Photoinduced by Eosin Decyl Ester. *Langmuir* (2020) doi:10.1021/acs.langmuir.0c01600.
55. Pereira, L. S. A. *et al.* Evidence of photoinduced lipid hydroperoxidation in Langmuir monolayers containing Eosin Y. *Colloids Surfaces B Biointerfaces* **171**, 682–689 (2018).
56. Bistaffa, M. J. *et al.* Photo-Induced Necrosis on Oropharyngeal Carcinoma (HEp-2) Cells Mediated by the Xanthene Erythrosine. *J. Nanosci. Nanotechnol.* **20**, 6180–6190 (2020).
57. Dix, T. A. & Aikens, J. Mechanisms and Biological Relevance of Lipid Peroxidation Initiation. *Chem. Res. Toxicol.* (1993) doi:10.1021/tx00031a001.
58. Robinson, M. A., Graham, D. J., Morrish, F., Hockenbery, D. & Gamble, L. J. Lipid analysis of eight human breast cancer cell lines with ToF-SIMS. *Biointerphases* (2016) doi:10.1116/1.4929633.
59. Robinson, M. A. Chemical Analysis of Cells and Tissues with Time-of-Flight Secondary Ion Mass Spectrometry. *ProQuest Dissertations and Theses* (2013).
60. Cai, Z. *et al.* Local Radiation Treatment of HER2-Positive Breast Cancer Using Trastuzumab-Modified Gold Nanoparticles Labeled with 177 Lu. *Pharm. Res.* **34**, 579–590 (2017).
61. Li, J. *et al.* In vitro cancer cell imaging and therapy using transferrin-conjugated gold nanoparticles. *Cancer Lett.* **274**, 319–326 (2009).
62. Kuo, W. S. *et al.* Gold nanomaterials conjugated with indocyanine green for dual-modality photodynamic and photothermal therapy. *Biomaterials* (2012) doi:10.1016/j.biomaterials.2012.01.035.
63. Shi, P. *et al.* pH-responsive NIR enhanced drug release from gold nanocages possesses high potency against cancer cells. *Chem. Commun.* (2012) doi:10.1039/c2cc33543c.
64. Wu, P., Gao, Y., Zhang, H. & Cai, C. Aptamer-guided silver-gold bimetallic nanostructures with highly active surface-enhanced Raman scattering for specific detection and near-infrared photothermal therapy of human breast cancer cells. *Anal. Chem.* (2012) doi:10.1021/ac3015164.
65. Krysko, D. V, Berghe, T. V., Herde, K. D. & Vandenabeele, P. Apoptosis and necrosis : Detection , discrimination and phagocytosis. *Methods* **44**, 205–221 (2008).
66. Hotchkiss, R. S., Strasser, A., McDunn, J. E. & Swanson, P. E. Cell Death. *N Engl J Med* **361**, 1570–1583 (2009).
67. Hou, L. *et al.* Necrotic pyknosis is a morphologically and biochemically distinct event from apoptotic pyknosis. *J Cell Sci.* **15**, 3084–3090 (2016).
68. Kroemer, G. *et al.* Classification of cell death: recommendations of the Nomenclature Committee on Cell Death 2009. *Cell Death Differ.* **16**, 3–11

(2009).
69. Poon, I. K. H., Hulett, M. D. & Parish, C. R. Molecular mechanisms of late apoptotic/necrotic cell clearance. *Cell Death and Differentiation* (2010) doi:10.1038/cdd.2009.195.
70. Riley, R. S. & Day, E. S. Gold nanoparticle-mediated photothermal therapy: applications and opportunities for multimodal cancer treatment. **9**, (2017).